Dual Buffering Inverse Design of Three-Dimensional Graphene-Supported Sn-TiO$_2$ Anodes for Durable Lithium-Ion Batteries

Jaegeon Ryu, Hyunji Kim, Jieun Kang, Hyunwoo Bark, Soojin Park,* and Hyunjung Lee*

Stable battery operation involving high-capacity electrode materials such as tin (Sn) has been plagued by dimensional instability-driven battery degradation despite the potentially accessible high energy density of batteries. Rational design of Sn-based electrodes inevitably requires buffering or passivation layers mostly in a multi-stacked manner with sufficient void inside the shells. However, undesirable void engineering incurs energy loss and shell fracture during the strong calendaring process. Here, this study reports an inverse design of freestanding 3D graphene electrodes sequentially passivated by capacity-contributing Sn and protective/buffering TiO$_2$. Monodisperse polymer bead templates coated with inner TiO$_2$ and outer SnO$_2$ layers generate regular macropores and 3D interconnected graphene framework while the inner TiO$_2$ shell turns inside out to fully passivate the surface of Sn nanoparticles during the thermal annealing process. The prepared 3D freestanding electrodes are simultaneously buffered by electronically conductive and flexible graphene support and ion-permeable/mechanically stable TiO$_2$ nanoshells, thus greatly extending the cycle life of batteries more than 5000 cycles at 5 C with a reversible capacity of ≈520 mAh g^{-1} with a high volumetric energy density.

1. Introduction

Lithium (Li) alloying anodes have been an active research avenue for developing high-energy-density lithium-ion batteries (LIBs) as a principal power source of electrified applications. Their high Li stoichiometry ($x > 3.0$ in Li$_x$M, M = Si, Ge, Sn, etc.)

Dr. J. Ryu, J. Kang, Prof. S. Park
Department of Chemistry
Division of Advanced Materials Science
Pohang University of Science and Technology (POSTECH)
Pohang 37673, Republic of Korea
E-mail: soojin.park@postech.ac.kr

H. Kim, Prof. H. Lee
School of Advanced Material Engineering
Kookmin University
Seoul 02707, Republic of Korea
E-mail: hyunjung@kookmin.ac.kr

Dr. H. Bark
School of Material Science and Engineering
Nanyang Technological University
50 Nanyang Avenue, Singapore 639798, Singapore

The ORCID identification number(s) for the author(s) of this article can be found under https://doi.org/10.1002/smll.202004861.

enables an improved specific capacity compared with that of conventional graphite anodes at low discharge potential below 1.0 V versus Li/Li$^+$.[1] Despite the electrochemical advantages of such alloying anodes, the use of Si or Ge-based anodes has been plagued by low electrical conductivity (≈10^3 S m^{-1}) and natural rarity in the metallic forms, respectively.[2] Instead, tin (Sn) anodes feature high electrical conductivity (≈10^7 S m^{-1}), comparable volumetric capacity (2020 mAh cm^{-3}), high availability, and versatility toward alkali metal-ion batteries, while large volumetric change (260% in Li$_{22}$Sn$_5$ corresponding to 994 mAh g^{-1}) of Sn anodes incurs structural collapse and consequent battery degradation.[3] Particle cracks accelerate the undesirable consumption of liquid electrolytes, thereby producing the thick solid electrolyte interphase (SEI) film and impeding the charge transport kinetics. Therefore, "mitigating" but not "circumvent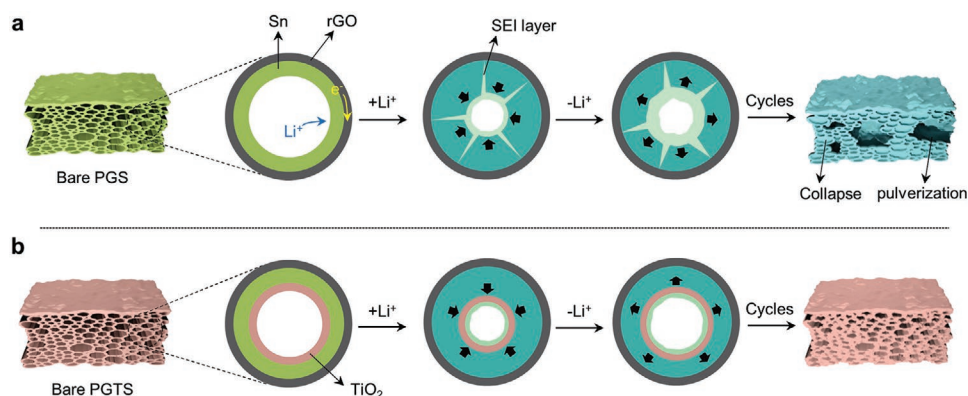ing" such unavoidable stress onto the Sn anodes is of great importance along with the stabilization of interface structure and the ensured electron/ionic transport pathway.[4]

Low dimensionality of Sn-based anodes (metallic or oxide forms) could reduce the risk of fracture and sustain the prolonged electrochemical cycling, especially at the nanoscale regime, including nanocrystal,[5] nanowires,[6] nanotubes (or hollow structure),[7] 3D structure,[8] core–shell,[9] and yolk–shell.[10] Otherwise, Sn-based binary (or intermetallic) compounds greatly promise the cycle stability and rate capability.[11] Supportive or buffering layers are essential even for such unique structures to mitigate the large volume change that mostly benefited from the electrically conductive carbon or mechanically stable TiO$_2$ polymorphs, for instance, highly conductive metallic Sn particles (20–50 nm) or its dispersion in the carbon nanofibers are protected by anatase TiO$_2$ spherical shell,[10b] or pipe-structured shell,[10a] respectively, during the battery operation. However, outermost nonconductive TiO$_2$ might slow down the electronic conduction over the composite electrodes or through the micrometer-long fibers, although it serves as a mechanically clamping layers as well as the artificial SEI layer to avoid direct contact of Sn anodes toward the liquid electrolytes. In this regard, the electrode architecture of Sn-based anodes should simultaneously utilize conductive carbon and protective TiO$_2$ skins in a balanced and well-controlled way.

ADVANCED
SCIENCE NEWS
www.advancedsciencenews.com

NANO · MICRO
small
www.small-journal.com

Scheme 1. Rational design of graphene-supported Sn-based composite electrodes. a) PGS electrode showing a fracture of Sn particles, the collapse of the porous structure, and loss of Sn particles from the graphene support with undesirable SEI accumulates to leave a substantial amount of residual Sn–Li. b) PGTS electrode showing ensured structural stability as dual-buffered by graphene support and TiO$_2$ shell for long-term battery operation without fracture or delamination.

High-volume-change electrode materials including Sn-based anodes mostly compromise the volumetric energy density of batteries due to the loss of dimensional stability (i.e., electrode swelling) even when integrated with polymeric binders that rather lower the energy density of batteries.[12] Instead of using such "electro-inactive" elements, freestanding 3D electrode architectures greatly enhance the volumetric energy density by excluding the polymeric binders and dispersing the active materials into the conductive carbon scaffolds such as carbon nanotubes (CNTs) or graphenes in their different forms (e.g., aerogels, films, sponges, etc.).[13] Among them, 3D porous graphene (PG) network (or film) ensures electron/ion transport through the open but continuous structure while the integration of active materials into the (porous) graphene films is only available through direct growth,[14] or confinement between the sheets.[15] As-formed freestanding hybrid electrodes are lack of controllability on the porosity that might lead to inhomogeneous ionic flux and show a plastic deformation during lithiation to lose the electronic conduction and eventual detachment of active materials. Thus, the rational design of the hybrid structure should consider the contact between the conductive network and active materials, and electrode integrity during electrochemical cycles by properly utilizing the porous structure.

Here, we report a rationally designed graphene-supported Sn-based composite structure for the stable Li-ion battery anodes (**Scheme 1**). Flexible 3D PG framework prepared via template method using monodisperse polystyrene (PS) ensures the continuous electronic conduction over the thick electrode and relieving stress caused by volume expansion of Sn. As introducing the redox-active SnO$_2$ shell on the template followed by thermal annealing, the inner surface of regular macropores (300 nm) is decorated with Sn nanoparticles that can contribute large capacities (denoted as PGS). However, such loosely anchored Sn nanoparticles are vulnerable to crack formation and fracture upon the lithium insertion, thus resulting in SEI accumulation on the surfaces to block the ionic transport and rapid battery degradation (Scheme 1a). Yet, dual layer-coated polymer templates (inner with TiO$_2$ and outer with SnO$_2$ on the PS) yield TiO$_2$ nanoshell-passivated PGS structure

(denoted as PGTS). During the lithiation and delithiation process, mechanically stable TiO$_2$ nanoshells reduce the risk of particle delamination as buffering inward and inhibit SEI thickening while maintaining the electronic conduction from the sustained flexible 3D graphene framework and ionic transport through the macropores (Scheme 1b). This dual-buffer strategy on the 3D freestanding electrode architecture greatly extended battery cycle life with a high volumetric capacity compared with conventional film-type electrode using high-capacity electrode materials.

2. Results and Discussion

As illustrated in **Figure 1**a, the preparation of PGTS films includes two stages of decorating TiO$_2$ and SnO$_2$ onto the PS particles in order (PS@TiO$_2$@SnO$_2$) and vacuum filtration of thereof graphene oxide (GO) solution for the fabrication of 3D freestanding films. The simple filtration is suited for the macroscopic assembly of GO/PS@TiO$_2$@SnO$_2$ sheets into the monolithic and interconnected network.[16] Subsequent thermal annealing results in the reduction of GO and SnO$_2$ to the thermally reduced GO (TrGO) and Sn, respectively, and removes the PS sacrificial template as simultaneously crystallizing the TiO$_2$ protective layers. In principle, the surface charge of the negatively charged PS template with anionic surfactant was modified as sufficiently positive (+56.7 mV) to drive the efficient adsorption of titanium precursors and uniform TiO$_2$ nanolayers onto the PS template by optimizing the concentration of ammonium ions (Figure S1 and Note S1, Supporting Information).[17] The resulting PS@TiO$_2$ particles were further coated with SnO$_2$ nanolayers by using diethylenetriamine (DETA) additives and SnO$_2$ precursors. One end group (i.e., amine) of DETA formed a ligand complex with Sn^{2+} ions while the other end group was attached to the hydroxyl group on the surface of TiO$_2$.[18]

The diameters of the spherical templates increased to 326 ± 7 and 377 ± 4 nm for PS@TiO$_2$ and PS@TiO$_2$@SnO$_2$, respectively, from the original PS (293 ± 7), as confirmed by dynamic light scattering (DLS) measurements (Figure S2a–d, Supporting Information). An energy-dispersive X-ray (EDS)
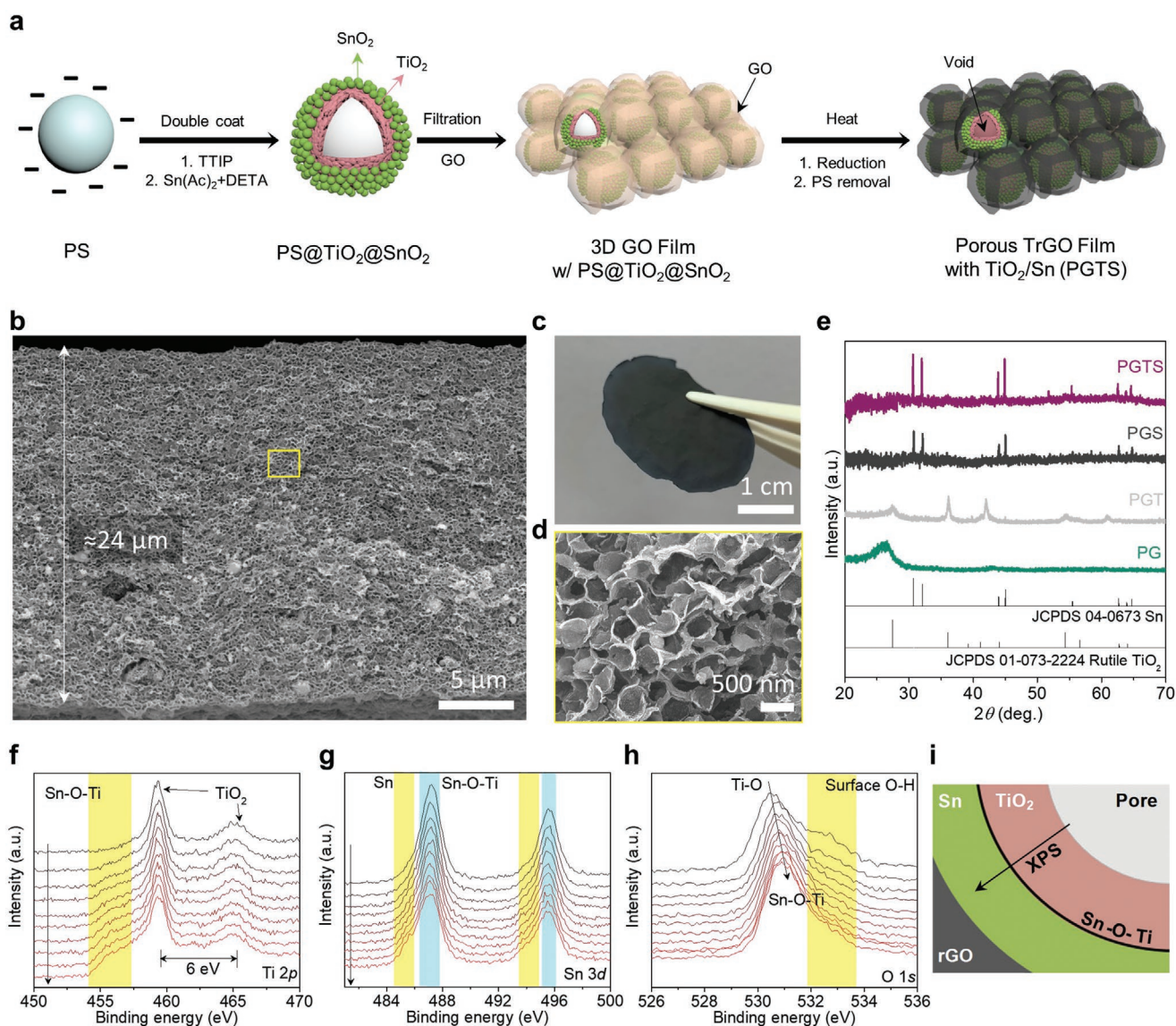
Figure 1. Preparation of PGTS electrode. a) Schematic illustration, b,d) cross-sectional SEM images, and c) digital photographs of PGTS electrodes. e) XRD patterns of different freestanding electrodes. XPS spectra of f) Ti 2p, g) Sn 3d, and h) O 1s of pristine PGTS electrode and i) schematic of expected interface structure of PGTS.

analysis found the layer-by-layer dual coating of TiO_2 and SnO_2. And, X-ray diffraction (XRD) patterns of PS@TiO_2 and PS@TiO_2@SnO_2 showed the amorphous nature of each oxide before thermal treatment but still, their mains peaks are well-matched with the reference peak position (JCPDS no. 41-144) as shown in Figure S3, Supporting Information. The relative composition of TiO_2 and SnO_2 can be simply controlled by increasing the concentration of the SnO_2 precursor at a given amount of PS@TiO_2 (Figure S4, Supporting Information). As the weight ratio of PS@TiO_2 to the SnO_2 precursors increased, the SnO_2 nanolayers fully covered the surface of PS@TiO_2 particles. However, above the critical concentration of the precursor (i.e., 1:1.5), isolated SnO_2 nanoparticles were observed (Figure S4e, Supporting Information). Besides, thermogravimetric analysis (TGA) results of each sample revealed a dramatic increase of

SnO_2 amounts in the composite template up to the weight ratio of 1:1 and thus such an optimized template with a uniform double-shell structure was used for further study (Figure S4f,g, Supporting Information). The weight ratio of TiO_2 and SnO_2 was directly related to the battery performance of PGTS, and the best performance was achieved at 1:1 of the weight ratio (Figure S5, Supporting Information). Sn-rich PGTS (≈PGS) with isolated Sn showed the rapidly decayed capacity caused by the structural collapse of the electrode during cycling, and Sn-less PGTS showed a low capacity due to the small amount of Sn.

Strong electrostatic interaction between the optimized PS@TiO_2@SnO_2 and GO formed a homogeneous solution and uniform assembly into the 3D porous structure after high-temperature annealing at an inert atmosphere without a trace

of severe agglomeration of Sn. A cross-sectional scanning electron microscopy (SEM) image showed a 24 µm-thick monolithic PGTS electrode of which the rGO framework retained 3D interconnections (Figure 1b,c). The regular porous structure is originated from the PS-based templates and their uniform pore size distribution ($\approx$300 nm) corresponds to the sacrificial space of the templates (Figure 1d). The thickness of the composite shell consisting of rGO frames ($\approx$5 nm) decorated with Sn and TiO_2 nanolayer is about 17 nm and transmission electron microscopy (TEM) images supported the designed structure with a uniform dispersion of Sn/TiO_2 (Figures S6 and S7, Supporting Information). TGA results under the air atmosphere revealed a chemical composition of the prepared PGTS electrode such that the contents of Sn, TiO_2, and TrGO were estimated as 18.8, 56.1, and 25.1 wt%, respectively, (Figure S8a and Note S2, Supporting Information).[10b,19]

Figure 1e shows the phase evolution of PG-based electrodes from the XRD patterns. The diffraction peak of (002) plane in the 3D rGO frameworks was consistently observed in all the electrodes as a shoulder peak at 25.4°, while the PGTS electrode involves both the tetragonal phase of reduced metallic Sn from SnO_2 and crystalized rutile phase of TiO_2 (JCPDS no. 04-0673 and 01-073-2224, respectively). The crystalline phases of rGO and Sn/TiO_2 were further validated by Raman analysis, which showed well-controlled incorporation of each component in the PGTS and control electrodes such as PG, PG/TiO_2 (PGT), and PG/Sn (PGS) (Figure S9, Supporting Information).
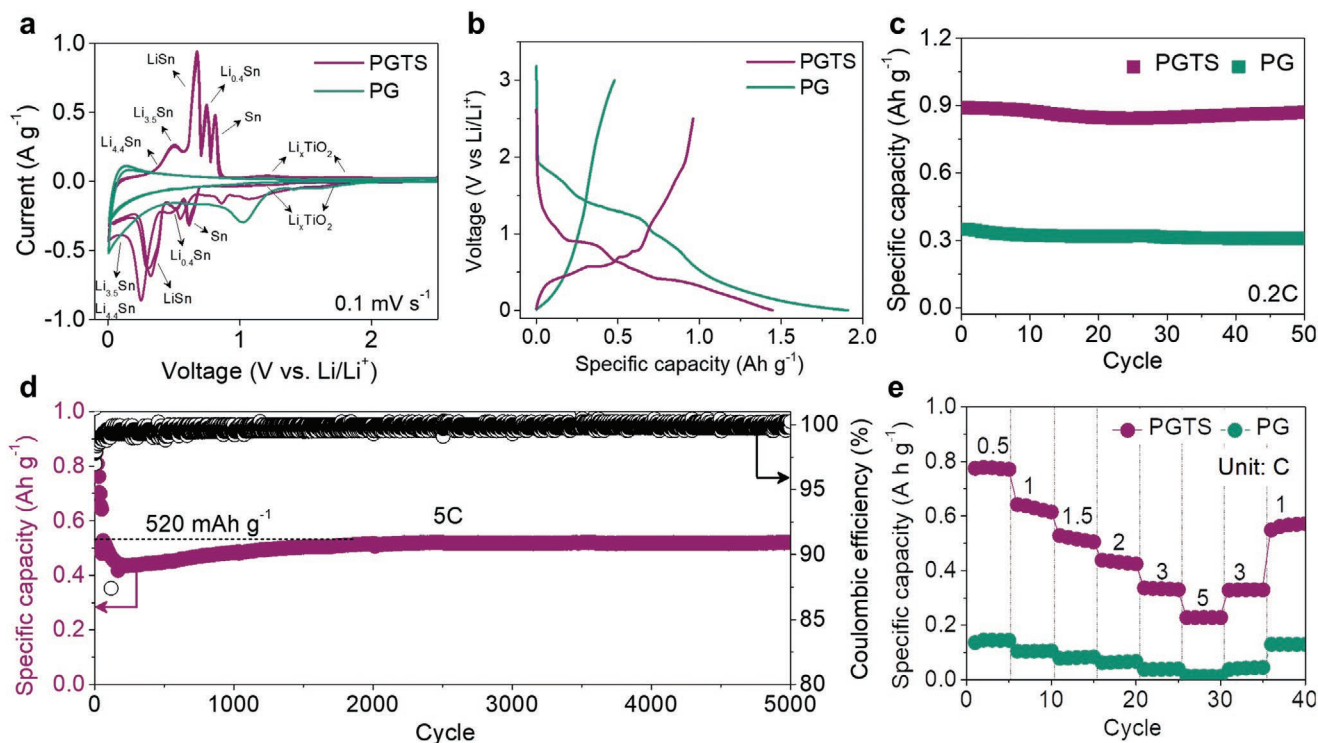
Unlike other composite electrodes using nanostructured Sn-based anodes cast on the metal current collectors, freestanding PGTS should be conductive to ensure the electronic conduction of the electrode during the battery operation. Uniform distribution of macropores reduced the differences between the in-plane and through-plane electrical conductivities and 3D interconnected structure of the prepared PGTS electrode as demonstrated previously[20] showed high electrical conductivity (10^2–10^6 S m^{-1}) that are highly comparable to other graphene-based scaffolds (Figure S10, Supporting Information).[13b,21] The utmost nonconductive TiO_2 shell will slow down the electron kinetics at the electrode–electrolyte interface to avoid substantial decomposition of the electrolytes as an effective protective layer. However, TiO_2 nanolayers allow for the Li-ion penetration,[22] while the electrons are sufficiently supplied from the inner rGO network to the in-between Sn. Ionic or electronic conduction from the dual buffer layers of TiO_2 and rGO, respectively, relieves the internal stress during lithiation and reduce the risk of detachment or pulverization. Also, the prepared PGTS film has intrinsic flexibility as shown in Figure S11a,b, Supporting Information.

X-ray photoelectron spectroscopy (XPS) depth-profiling results showed the chemical nature and interface structure of the PGTS electrode (Figure 1f–i). In Ti 2p spectra, two protruding peaks at 458.7 eV (Ti $2p_{3/2}$) and 464.9 eV (Ti $2p_{1/2}$) correspond to the Ti^{4+} in TiO_2 with a typical gap of 6 eV and decreasing intensities according to the profiling depth (Figure 1f). Close to the interface of the TiO_2 outer shell and metallic Sn inner shell, a new peak evolved at the lower binding energy of 454.1–457.2 eV that is related to the Sn–O–Ti combination. A similar coordinated interface structure was also observed in the Sn 3d spectra (Figure 1g). Importantly,

metal–oxygen binding energy was shifted positively from the typical Ti−O bonds to Sn–O–Ti owing to the higher electronegativity of Sn atoms compared with that of Ti (Figure 1h).[23] The protective TiO_2 shell that has an intimate junction with inner high-capacity Sn anodes will greatly improve the structural stability of the PGTS electrode over the electrochemical cycles. Please note that the existence of the Sn−O−Ti interface in the PGTS electrode might enhance the thermal stability and cause some deviations in the calculation of Sn contents from the TGA results.[24]

The prepared PGTS and control electrodes were electrochemically evaluated by assembling the coin-type half cells as paired with lithium metal reference/counter electrodes. We first investigated the redox activity of the electrodes by cyclic voltammetry (CV) (**Figure 2**a; Figure S12a, Supporting Information). PG electrode without inorganic electroactive materials showed a typical capacitor-like behavior that relied on the adsorption-desorption of Li-ions on the surface along with the electrolyte decomposition at the first cathode scan. Similar pseudocapacitive charge storage occurred on the PGT electrode without discernible peaks.[25] As the metallic Sn was involved in the electrodes (PGS or PGTS), distinctive redox pairs in the cathodic and anodic scans were observed that are associated with the lithiation/delithiation process of typical Sn anodes below 1.0 V and above 0.3 V versus Li/Li$^+$, respectively.[3] Redox peaks corresponding to Li–Sn alloy phases of $Li_{4.4}Sn$, $Li_{3.5}Sn$ (0.5 V), LiSn (0.68 V), $Li_{0.4}Sn$ (0.74 V), and Sn (0.8 V) were developed in order. The broad peaks in 0.8–1.5 V and 1.7–2.2 V regions indicate the lithiation/delithiation of rutile TiO_2. Highly porous and conductive rGO framework (PG) irreversibly consumed Li-ions mostly for the SEI formation at the first galvanostatic cycle 0.05 C, thus delivering a charge capacity of 480 mAh g^{-1} and the corresponding ICE of 25.1% (Figure 2b; Figure S12b, Supporting Information). The heavy TiO_2 with low Li stoichiometry contributed negligible specific capacity to the PGT electrode and rather lowered its capacity to 400 mAh g^{-1} with ICE of 24.3%. It is noted that pseudocapacitive charge storage is suited for the fast-charging condition but not for high-energy systems.[26] Comparing the reversible capacities and compositions of PG and PGT electrodes, we can estimate the charge capacity of TiO_2 in the PG-based electrodes as 188 mAh g^{-1} (Figure S8b, Supporting Information).

Incorporation of Sn anodes into the capacitive PG framework increased the initial reversibility and thus the reversible capacity of 1210 and 960 mAh g^{-1} in PGS and PGTS electrodes, respectively. However, PGS and PGTS electrodes showed relatively low ICEs of 74.1% and 66.4%, respectively. The prelithiation method improved the ICE of PGTS to 92.4%, addressing relatively low ICEs of rGO-based composite materials (Figure S13, Supporting Information). Compared with PG and PGT electrodes that showed a limited yet stable capacity of less than 350 mAh g^{-1} during the subsequent cycles at 0.2 C, the PGS electrode rapidly degraded in 10 cycles in the absence of the TiO_2 nanolayers (Figure 2c; Figure S12c, Supporting Information). Ex situ analysis of the PGS electrode after the cycles revealed that the collapsed porous structure and agglomerated or detached Sn nanoparticles changed to an electrochemically "dead site" along with excessively deposited SEI films on the electrode (Figure S14, Supporting Information). Interestingly,

**ADVANCED
SCIENCE NEWS**

www.advancedsciencenews.com

**NANO · MICRO
small**

www.small-journal.com

Figure 2. Battery performances of PGTS film. a) Cyclic voltammograms, b) initial discharge–charge voltage profiles at 0.05 C, and c) capacity retention at 0.2 C of PG and PGTS electrodes. d) Long-term stability of PGTS electrode for 5000 cycles at 5 C. e) Rate capability results of PG and PGTS electrodes at various C-rates.
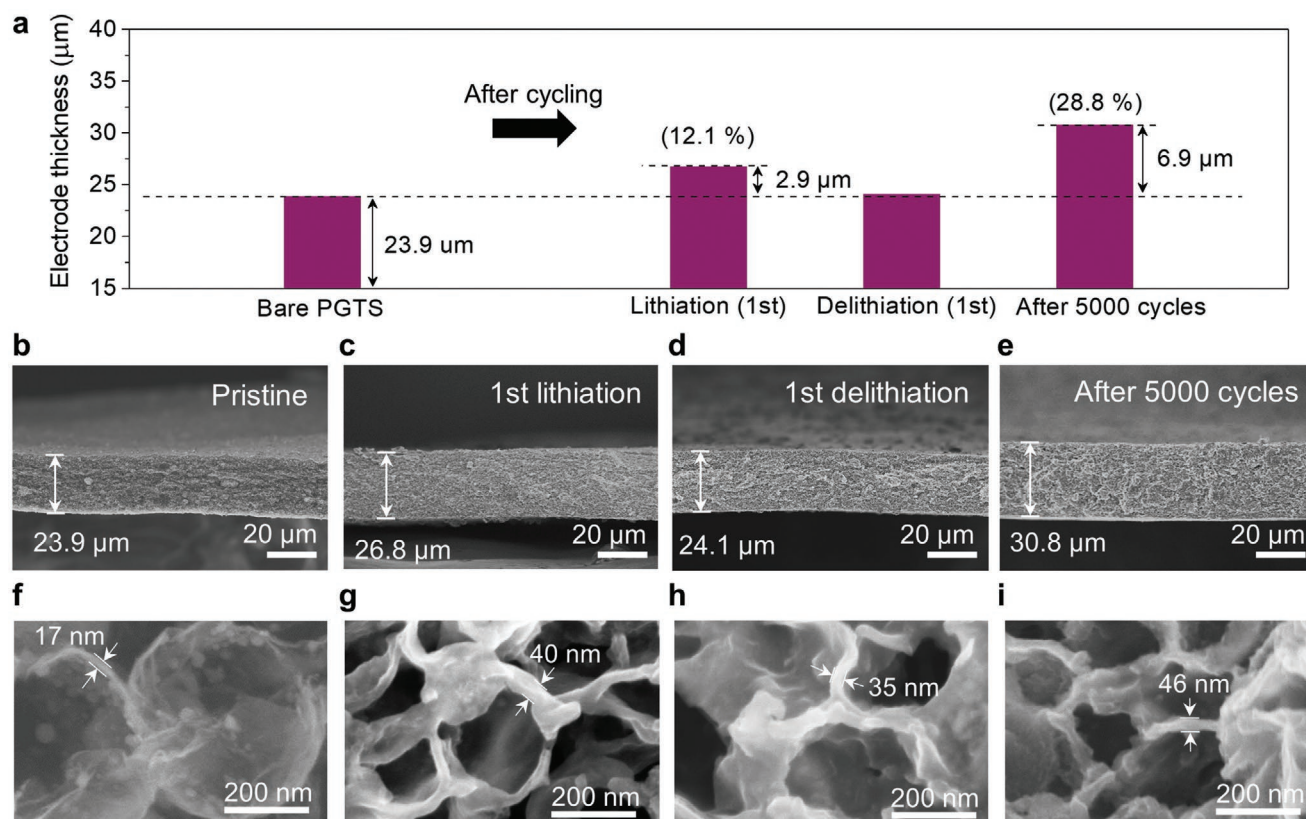
the PGTS electrode showed 100% capacity retention at 0.2 C for 50 cycles due to the dual buffering effect of the inner electron-conductive rGO and outer ion-permeable TiO_2 (Figure 2c). The PGTS electrode was further tested at 5.0 C for 5000 cycles to demonstrate a durable structure for the reliable battery operation (Figure 2d). Despite initial polarization from freestanding architecture without metal current collectors at the increased current densities (Figure 2e), the reversible capacities gradually increased to 520 mAh g^{-1} at 5.0 C and showed no capacity decay in further cycles. The full recovery of reversible capacities after the rate capability test supported the well-integrated structure of the PGTS electrode.

To validate our design in terms of the retained capacity and cycle life at the different C-rates, the comparative plot of various graphene-based freestanding electrodes using the Sn-based anodes was provided, which showed outstanding cycle stability and high capacity in the PGTS electrode (Figure S15, Supporting Information). Although there are reported promising designs to utilize Sn anodes and achieve decent battery performances, most strategies required intricate preparation steps,[5b,27] and still evaluated in the form of slurry-cast composite electrodes that are out of scope in this study. Dimensional stability of freestanding electrode involving the large-volume-change materials is of crucial importance to compete with the conventional thick composite electrode in terms of volumetric capacity. As summarized in **Figure 3**a, the electrode swelling in the vertical direction was highly suppressed as low as 12.1% at the first lithiation and recovered to the initial thickness of ≈24 µm upon delithiation. Even after the repeated 5000 cycles, the thickness

of the PGTS electrode remained as 28.8% swelled state without delamination or microcracks of which volume expansion falls in the safe and affordable range of volumetric margins in the cylindrical cells (Figure 3b–e).[28] The flexibility of PGTS was also maintained (Figure S11c,d, Supporting Information).

High-magnification SEM images showed the change in the total thickness of electroactive shells during the cycles. The lithiated shells considerably expanded as high as 130% of the initial structure but no disconnections were observed (Figure 3f,g). Instead, the entire network reconfigured the porous structure upon the lithiation such that uniform rGO-based shells turned into a partial buckling structure due to the large volume change of Sn as recently observed in the case of Si anodes.[29] As relieving the internal stress by the ripple formation and simultaneously inward expansion,[30] the size of void space decreased while sustaining the interconnected 3D structure. After the subsequent delithiation and long-term cycles, the buckling behavior improved and the cycled PSTS electrode retained open structure toward the electrolyte infiltration (Figure 3h,i). It is noted that the displayed thickness involves the SEI layers since the acid-leaching of SEI layers might damage the overall structure and weaken our conclusion. This self-reconfigured 3D structure based on the rGO framework decorated with high-capacity Sn and protective TiO_2 could provide a mechanically robust platform for the design of Li-alloying anode in the freestanding form.

The structural stability of large-volume-change electrode materials strongly correlates to the stability of interface films, SEI layers, and charge transport kinetics. Nyquist plots of the

**ADVANCED
SCIENCE NEWS**

www.advancedsciencenews.com
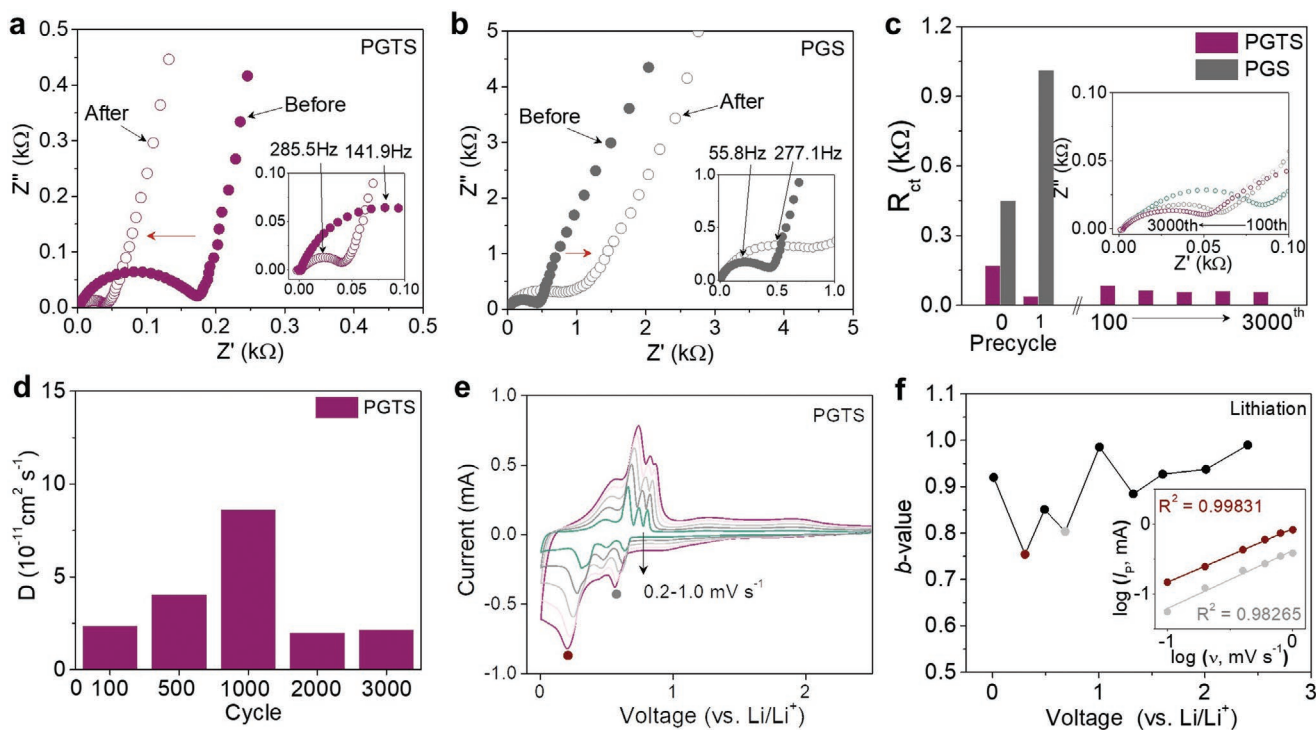
NANO · MICRO

small

www.small-journal.com

Figure 3. Dimensional stability results of PGTS film. a) Thickness change of PGTS electrode over 5000 cycles. b–e) Cross-sectional and f–i) enlarged SEM images of PGTS electrode before the cycle, after first lithiation, first delithiation, and 5000 cycles, respectively, in order.

PGTS and control electrodes obtained from the electrochemical impedance spectroscopy (EIS) measurements showed significant differences during the first cycle (**Figure** 4a,b; Figure S16a–c, Supporting Information). Highly electron-conducting PG electrode has the lowest charge transfer resistance (R_{ct}) according to the equivalent circuit model before the formation cycle along with the capacitive nature at the low-frequency region (large slope at the tail) (Figure S16b, Supporting Information). The accumulated ready-to-react electrons on the large surface area of the 3D rGO framework formed a thick SEI layer with an increased R_{ct}. Despite large R_{ct} in the insulating TiO_2-decorated PG electrode (PGT), such a protective but ion-permeable shell induced a uniform SEI formation (Figure S16c, Supporting Information). In the same manner, the R_{ct} of the PGTS electrode greatly decreased after the SEI formation, thus suggesting that the regulated electron kinetics by TiO_2 promoted the homogeneous interface film formation while maintaining the structural integrity (Figure 4a). However, the decorated Sn that is vulnerable to detachment and pulverization in the PGS electrode disturbed the uniform SEI formation and showed a large R_{ct} before and after the first cycle (Figure 4b). Importantly, the PGTS electrode showed a stable and rather lower R_{ct} as the cycles proceeded, of which results are closely associated with the deformed buckling structure to stabilize the interface and reduce the risk of losing active materials (Figure 4c). From the ex situ XPS results of the PGTS electrode (Figure S17, Supporting Information), the PGTS electrode

still retained the intimate contact of Sn and TiO_2 and showed uniform SEI structure upon the probed depth.

Based on the Li-ion diffusion model using the Warburg factors,[31] Li-ion diffusion coefficient (D_{Li^+}) of the PGTS electrode was calculated from the EIS analysis at the different stages of cycling (Figure 4d; Figure S16d, Supporting Information). Typical diffusivity of Li-ions in the nanocrystalline Sn anodes was reported as 8×10^{-8}–5.9×10^{-7} cm^{-2} s^{-1}.[32] Although a certain portion of low-diffusivity TiO_2 ($\approx 10^{-14}$ cm^2 s^{-1} along the c-axis and $\approx 10^{-6}$ cm^2 s^{-1} in the ab-plane) was involved in the PGTS electrode,[33] the calculated D_{Li^+} fall in the reasonable range of 1.9–8.6×10^{-11} cm^2 s^{-1} that is comparable to or higher than other Sn-based anodes.[3] As recently investigated in various electrode materials, diffusivity of Li-ions in the host structures can be estimated by varying the scan rates during the CV measurements where the calculated D_{Li^+} based on the Randles–Sevcik equation are similar to those from the above model (Figure 4e). Besides, such estimations provide a crucial information about relative portion of two charge storage mechanisms of diffusion-controlled (faradaic) or capacitive (non-faradaic) reactions from the following equation: $i = k_1 v + k_2 v^{1/2} = av^b$, where k_1, k_2, and a are the constants; v is the scan rate; and b is a value ranging from 0.5 (fully faradaic) to 1.0 (fully non-faradaic). Except for the representative redox voltages of Sn–Li alloying reaction at 0.21 and 0.56 V (Figure 4f), most b values are well above 0.8, which implies that the pseudocapacitive contribution from the TiO_2

**ADVANCED
SCIENCE NEWS**

www.advancedsciencenews.com

NANO · MICRO

small

www.small-journal.com

Figure 4. Interface analysis and diffusion kinetics of PGTS film. EIS Nyquist plots of a) PGTS and b) PGS electrodes before and after the first cycle. c) Change in the charge transfer resistance of PGS and PGTS electrodes during the cycles (inset: corresponding Nyquist plots during cycles). d) Calculated Li-ion diffusion coefficients (D_{Li^+}) from the EIS analysis during the cycles. e) CV curves at different scan rates and f) corresponding b-value plots of the PGTS electrode (inset: peak current vs scan rate plots).

and rGO framework enhanced the charge transport kinetics of Sn in the PGTS electrode.

3. Conclusion

Freestanding electrode architecture provides a versatile platform to innovate the state-of-the-art rechargeable batteries as replacing heavy and thick current collectors by a lightweight and compact carbon-based counterpart while integrating the Sn anodes. In this work, we demonstrated how to effectively incorporate the high-capacity yet large-volume-change Sn anodes into the PG-based scaffold by utilizing the sacrificial templating method. Double-shelled monodisperse PS templates carried Sn and TiO_2 intermediates to the graphene scaffold and simultaneously served as a porogen to produce a 3D porous structure. Thermally induced formation of capacity-contributing Sn and protective TiO_2 nanoshells tightly adhered to the porous 3D rGO scaffold with homogeneous macropores. The inner rGO scaffold and outer TiO_2 enabled uniform diffusion of electrons and Li-ions, respectively, along with the dual buffering effects from the two functional layers. The flexible nature of the rGO framework allowed stress-relieving deformation (rippling) of the PGTS structure to ensure structural stability and TiO_2 nanoshells promoted the formation of stable SEI structure, thus realizing long-term battery operation over thousands of cycles with a negligible volumetric change or degradation of the electrode. The validated design rationales can be extended to stabilize

other monolithic electrodes involving the high-capacity electrode materials for the rechargeable batteries beyond Li.

4. Experimental Section

Materials: Divinylbenzene (DVB), sodium dodecyl sulfate (SDS), titanium isopropoxide (TTIP, 97%), and tin acetate dihydrate were purchased from Sigma-Aldrich. DETA was purchased from TCI and ammonia solution (30%) was purchased from Samchun Chemicals. Styrene, potassium persulfate (PPS), anhydrous ethanol (99.9%), acetonitrile, isopropyl alcohol, and acetic acid were purchased from Daejung Chemicals. To obtain graphene (GO), commercial graphite power (SP-1, BAY CARBON, Inc., USA) was purchased.

Preparation of PS Spheres: PS spheres as sacrificial agents were prepared for porous structure in film. First, styrene and DVB were used as the monomer and PPS and SDS as an anionic initiator and a surfactant, respectively. After stabilizing deionized (DI) water (36 mL) by purging N_2 at 70 °C for 1 h, 0.2×10^{-3} M of SDS and 10×10^{-3} M of PPS were added step by step. Then, 3.0 M of styrene that was filtered through activated alumina in advance, and that of 10 mol% DVB mixture was dropped slowly. After emulsion polymerization for 4 h, the samples were washed by DI water several times for 7–10 days.

Preparation of PS@TiO₂ and PS@SnO₂: The coating process was performed in the cosolvent of ethanol and acetonitrile while hydrolyzing TTIP in the presence of ammonia as a catalyst. In particular, 0.168 g of PS particles was dispersed in 100 mL of ethanol/acetonitrile (3:1 v/v) and then mixed with 0.3 mL ammonia solution at room temperature. Finally, 0.5 mL TTIP in 20 mL of ethanol/acetonitrile (3:1 v/v) was added to the above PS suspension under stirring as increasing the temperature to 60 °C. After the reaction for 1 h, the synthesized particles were thoroughly rinsed by ethanol.[17] For PS@SnO₂, 0.3 g of PS particles was added into a 0.054 M solution of tin acetate dihydrate in ethanol

ADVANCED
SCIENCE NEWS

www.advancedsciencenews.com

NANO · MICRO
small
www.small-journal.com

(37.5 mL) under stirring at 60 °C for 90 min. Then, 3.7×10^{-3} M of ammonia solution in ethanol was added to the above suspension, and the mixture was stirred at 60 °C for 3 h and then the PS@SnO$_2$ particles were collected and washed with ethanol.[34]

Preparation of PS@TiO$_2$@SnO$_2$: In practice, 20 mg of tin acetate dihydrate was dissolved in 20 mL IPA under stirring at 60 °C and then dissolved with different amounts (10, 16, 20, 26.6, 30 mg) of PS@TiO$_2$ particles. After adding 30 μL DETA to the above-monodispersed solution and aging for 1 h, 20 mL of the mixture was transferred to a Teflon-lined autoclave and kept in an oven at 200 °C for 2 h. After naturally cooling down to room temperature, the yellow-colored precipitate was collected and washed with ethanol.[35]

Preparation of PGTS Film: GO was prepared via Hummer's method from graphite powder.[36] Briefly, 2 g of graphite and 1 g of NaNO$_3$ was added into 50 mL of H$_2$SO$_4$ under stirring for 1 h with the flask kept in an ice bath (0 °C). Afterward, 6 g of KMnO$_4$ was added in the above mixture, and the temperature was gradually increased up to 35 °C. Then, 92 mL of H$_2$O was added to the mixture slowly, followed by the addition of a mixture of H$_2$O and H$_2$O$_2$ (280 and 5 mL) for the termination of the reaction. The mixture was cleaned with a 10% HCl solution and DI water. Finally, the product was freeze-dried to obtain graphite oxide powders. To prepare GO solution with 1 mg mL^{-1} concentration, 500 mg of graphite oxide powder was put into 500 mL of H$_2$O with an ultrasonic horn sonicator for 1 h at room temperature. After the dispersion and purification by centrifugation at 3000 rpm for 5 min, the clear dark brown supernatant (GO solution) was obtained. For the preparation of thermally reduced graphene oxide film with a continuous and porous structure, pH control is critical.[16b] The synthesized core/double-shell particles and GO solid from as-prepared GO suspensions (1 mg mL^{-1}) were mixed with a 3:1 w/w ratio and dispersed into DI water where the controlled pH values were 10–11. The 3D films as PS@TiO$_2$@SnO$_2$-GO were produced by vacuum filtration through a polytetrafluoroethylene (PTFE) membrane (0.2 μm, $\varphi = 47$ mm, Wattman). After filtrations, the pH of the solution was adjusted by an acetic acid solution to result in electrostatic interactions between core/double-shell particles and GO, thereby rendering the peel-off process much easier from the membrane. The final films were thermal-annealed under Ar gas at 1000 °C for 1 h with a ramping rate of 5 °C min^{-1} to produce PG, PGT, PGS, and PGTS films, depending on the target particles.

Physicochemical Characterization: The morphology and element analysis of all the samples were performed by field-effect scanning electron microscopy (FE-SEM, JSM-7610F, JOEL) under 5–15 kV. The size distribution of PS, PS@TiO$_2$, and PS@TiO$_2$@SnO$_2$ particles, and zeta potential of PS particles were measured by DLS (Nicomp 380 ZLS) devices. The lattice structure of prepared samples was confirmed by X-ray diffractometer (D/MAX 2500, Rigaku, Japan) with Cu Kα beam ($\lambda = 1.54$ Å) in the 2θ range of 20–80°. The weight ratio of prepared samples was analyzed by thermogravimetry analyzer (Mettler Toledo, TGA/DSC 1). The Raman spectra of samples were obtained by Raman spectrometer (LabRAM HR800UV). The PGTS films were analyzed by XPS (K-alpha, Thermo Fisher) depth profiling with an ion beam to etch 50 nm in intervals of 5 nm. To investigate an in-plane and out-of-plane of conducting property in sample films, the contact electrode was loaded on the side, top, and bottom sheet by masking with liquid metal (gallium-indium eutectic, Sigma-Aldrich). A sheet resistance was obtained from a current–voltage measurement by using the current source meter (Keithley 2400) contacted to the liquid metal on the sheet. The sheet resistance was converted into electrical conductivity with dimensional factors. The TEM analysis was performed using a JEM-2100F (with Cs corrector on STEM, JEOL).

Battery Evaluation: The freestanding films manufactured without additional carbon black and binder were cut into the disc-type electrodes with a diameter of 10–14 mm. The coin cell assembly was carried out inside the Ar-filled glove box with the lithium metal as a reference/counter electrode and microporous separator. The liquid electrolyte used in this study consists of 1.3 M lithium hexafluorophosphate (LiPF$_6$) in the ethylene carbonate (EC) and diethylene carbonate (DEC) with a 10 wt% fluoroethylene carbonate (FEC). After aging at 40 °C for 2 h, the assembled cells were analyzed through the galvanostatic battery cycler (Wonatech) and potentiostat (Biologic) for the CV and EIS with a potential window of 0.005–2.5 V at 0.1 mV s^{-1} and 100 kHz–0.1 Hz with an amplitude of 10 mV, respectively.

Supporting Information

Supporting Information is available from the Wiley Online Library or from the author.

Conflict of Interest

The authors declare no conflict of interest.

[1] a) W.-J. Zhang, *J. Power Sources* **2011**, *196*, 13; b) J. Ryu, D. Hong, H. W. Lee, S. Park, *Nano. Res.* **2017**, *10*, 3970; c) J. Ryu, W. J. Song, S. Lee, S. Choi, S. Park, *Adv. Funct. Mater.* **2020**, *30*, 1902499.

[2] a) L. C. Loaiza, L. Monconduit, V. Seznec, *Small* **2020**, *16*, 1905260; b) J. Ryu, J. H. Seo, G. Song, K. Choi, D. Hong, C. Wang, H. Lee, J. H. Lee, S. Park, *Nat. Commun.* **2019**, *10*, 2351; c) G. Song, J. Y. Cheong, C. Kim, L. L. Luo, C. Hwang, S. Choi, J. Ryu, S. Kim, W. J. Song, H. K. Song, C. Wang, I. D. Kim, S. Park, *Nat. Commun.* **2019**, *10*, 2364.

[3] H. Ying, W.-Q. Han, *Adv. Sci.* **2017**, *4*, 1700298.

[4] B. Wang, B. Luo, X. Li, L. Zhi, *Mater. Today* **2012**, *15*, 544.

[5] a) Y. Xu, Q. Liu, Y. Zhu, Y. Liu, A. Langrock, M. R. Zachariah, C. Wang, *Nano Lett.* **2013**, *13*, 470; b) R. Mo, X. Tan, F. Li, R. Tao, J. Xu, D. Kong, Z. Wang, B. Xu, X. Wang, C. Wang, J. Li, Y. Peng, Y. Lu, *Nat. Commun.* **2020**, *11*, 1374.

[6] P. Meduri, C. Pendyala, V. Kumar, G. U. Sumanasekera, M. K. Sunkara, *Nano Lett.* **2009**, *9*, 612.

[7] a) J. Pu, H. Du, J. Wang, W. Wu, Z. Shen, J. Liu, H. Zhang, *J. Power Sources* **2017**, *360*, 189; b) N. Wu, W. Du, X. Gao, L. Zhao, G. Liu, X. Liu, H. Wu, Y.-B. He, *Nanoscale* **2018**, *10*, 11460.

[8] P. Sun, J. Davis, L. Cao, Z. Jiang, J. B. Cook, H. Ning, J. Liu, S. Kim, F. Fan, R. G. Nuzzo, P. V. Braun, *Energy Storage Mater.* **2019**, *17*, 151.

[9] B. Luo, B. Wang, M. Liang, J. Ning, X. Li, L. Zhi, *Adv. Mater.* **2012**, *24*, 1405.

[10] a) M. Mao, F. Yan, C. Cui, J. Ma, M. Zhang, T. Wang, C. Wang, *Nano Lett.* **2017**, *17*, 3830; b) S. Kang, X. Chen, J. Niu, *Nano Lett.* **2018**, *18*, 467; c) W.-M. Zhang, J.-S. Hu, Y.-G. Guo, S.-F. Zheng, L.-S. Zhong, W.-G. Song, L.-J. Wan, *Adv. Mater.* **2008**, *20*, 1160; d) K. T. Lee, Y. S. Jung, S. M. Oh, *J. Am. Chem. Soc.* **2003**, *125*, 5652.

ADVANCED
SCIENCE NEWS

www.advancedsciencenews.com

NANO · MICRO
small
www.small-journal.com

[11] a) M.-G. Park, D.-H. Lee, H. Jung, J.-H. Choi, C.-M. Park, *ACS Nano* **2018**, *12*, 2955; b) Y. Wang, J. Y. Lee, *Angew. Chem., Int. Ed.* **2006**, *45*, 7039; c) B. T. Heligman, K. J. Kreder, A. Manthiram, *Joule* **2019**, *3*, 1051; d) P. Nithyadharseni, M. V. Reddy, B. Nalini, M. Kalpana, B. V. R. Chowdari, *Electrochim. Acta* **2015**, *161*, 261.

[12] a) J. Ryu, S. Kim, J. Kim, S. Park, S. Lee, S. Yoo, J. Kim, N.-S. Choi, J.-H. Ryu, S. Park, *Adv. Funct. Mater.* **2020**, *30*, 1908433; b) S. Choi, T.-W. Kwon, A. Coskun, J. W. Choi, *Science* **2017**, *357*, 279.

[13] a) B. Wang, J. Ryu, S. Choi, G. Song, D. Hong, C. Hwang, X. Chen, B. Wang, W. Li, H.-K. Song, S. Park, R. S. Ruoff, *ACS Nano* **2018**, *12*, 1739; b) J. Ryu, B. Park, J. Kang, D. Hong, S.-D. Kim, J.-K. Yoo, J. W. Yi, S. Park, Y. Oh, *ACS Nano* **2019**, *13*, 14357; c) B. Luo, T. Qiu, B. Wang, L. Hao, X. Li, A. Cao, L. Zhi, *Nanoscale* **2015**, *7*, 20380.

[14] C. Zhou, J. Liu, S. Guo, P. Zhang, S. Li, Y. Yang, J. Wu, L. Chen, M. Wang, *ChemElectroChem* **2020**, *7*, 1573.

[15] a) K. Zhang, Y. Xia, Z. Yang, R. Fu, C. Shen, Z. Liu, *RSC Adv.* **2017**, *7*, 24305; b) X. Yao, Y. Zhao, *Chem* **2017**, *2*, 171.

[16] a) B. G. Choi, J. Hong, W. H. Hong, P. T. Hammond, H. Park, *ACS Nano* **2011**, *5*, 7205; b) B. G. Choi, M. Yang, W. H. Hong, J. W. Choi, Y. S. Huh, *ACS Nano* **2012**, *6*, 4020.

[17] P. Wang, D. Chen, F.-Q. Tang, *Langmuir* **2006**, *22*, 4832.

[18] a) H. Peng, X. Yang, P. Zhang, Y. Zhang, C. Liu, D. Liu, J. Gui, *RSC Adv.* **2017**, *7*, 50216; b) Y.-X. Zhang, X. Guo, X. Zhai, Y.-M. Yan, K.-N. Sun, *J. Mater. Chem. A* **2015**, *3*, 1761.

[19] J. Qin, C. He, N. Zhao, Z. Wang, C. Shi, E.-Z. Liu, J. Li, *ACS Nano* **2014**, *8*, 1728.

[20] H. Bark, J. Lee, H. Lim, H. Y. Koo, W. Lee, H. Lee, *ACS Appl. Mater. Interfaces* **2016**, *8*, 31617.

[21] M. A. Worsley, P. J. Pauzauskie, T. Y. Olson, J. Biener, J. H. Satcher, T. F. Baumann, *J. Am. Chem. Soc.* **2010**, *132*, 14067.

[22] Y. Jin, S. Li, A. Kushima, X. Zheng, Y. Sun, J. Xie, J. Sun, W. Xue, G. Zhou, J. Wu, F. Shi, R. Zhang, Z. Zhu, K. So, Y. Cui, J. Li, *Energy Environ. Sci.* **2017**, *10*, 580.

[23] B. Sun, T. Shi, Z. Peng, W. Sheng, T. Jiang, G. Liao, *Nanoscale Res. Lett.* **2013**, *8*, 462.

[24] W. Si, H. Liu, T. Yan, H. Wang, C. Fan, S. Xiong, Z. Zhao, Y. Peng, J. Chen, J. Li, *Appl. Catal., B* **2020**, *269*, 118797.

[25] W. Wen, J.-M. Wu, Y.-Z. Jiang, L.-L. Lai, J. Song, *Chem* **2017**, *2*, 404.

[26] J. Ding, W. Hu, E. Paek, D. Mitlin, *Chem. Rev.* **2018**, *118*, 6457.

[27] Y. Li, C. Ou, J. Zhu, Z. Liu, J. Yu, W. Li, H. Zhang, Q. Zhang, Z. Guo, *Nano Lett.* **2020**, *20*, 2034.

[28] M. Ko, S. Chae, J. Ma, N. Kim, H.-W. Lee, Y. Cui, J. Cho, *Nat. Energy* **2016**, *1*, 16113.

[29] X. Xia, A. Afshar, H. Yang, C. M. Portela, D. M. Kochmann, C. V. Di Leo, J. R. Greer, *Nature* **2019**, *573*, 205.

[30] J. Ryu, T. Chen, T. Bok, G. Song, J. Ma, C. Hwang, L. Luo, H.-K. Song, J. Cho, C. Wang, S. Zhang, S. Park, *Nat. Commun.* **2018**, *9*, 2924.

[31] C. Ho, *J. Electrochem. Soc.* **1980**, *127*, 343.

[32] J. Shi, Z. Wang, Y. Q. Fu, *J. Mater. Sci.* **2016**, *51*, 3271.

[33] P. Kubiak, M. Pfanzelt, J. Geserick, U. Hörmann, N. Hüsing, U. Kaiser, M. Wohlfahrt-Mehrens, *J. Power Sources* **2009**, *194*, 1099.

[34] M. del Rio, C. Palomino Cabello, V. Gonzalez, F. Maya, J. B. Parra, V. Cerdà, G. Turnes Palomino, *Chem. - Eur. J.* **2016**, *22*, 7533.

[35] A. Pang, X. Sun, H. Ruan, Y. Li, S. Dai, M. Wei, *Nano Energy* **2014**, *5*, 82.

[36] W. S. Hummers, R. E. Offeman, *J. Am. Chem. Soc.* **1958**, *80*, 1339.